



# Creep Deformation and Gas Permeability in Fractured Claystone Under Various Stress States

X. Chen<sup>1,2</sup> · S. Y. Xie<sup>2</sup> · W. Zhang<sup>2</sup> · G. Armand<sup>3</sup> · J. F. Shao<sup>1,2</sup>

Received: 12 July 2021 / Accepted: 31 December 2021 / Published online: 14 January 2022  
© The Author(s), under exclusive licence to Springer-Verlag GmbH Austria, part of Springer Nature 2022

## Abstract

Clayey rocks with low permeability are investigated as a potential geological barrier for underground disposal of radioactive waste. Subjected to thermo-hydromechanical loads, damaged zones can be created around underground structures. It is crucial to investigate the evolution of permeability in those critical zones. In this study, an original experimental study is performed on the Callovo-Oxfordian (COx) claystone investigated in the French radioactive waste disposal project. A cylindrical sample is first subjected to a confining pressure, then to different values of shear stress until the creation of a planar fracture along the height. Creep tests are conducted under the different steps of shear stress. Gas permeability is also measured during the creep phases. Unloading–reloading steps of confining pressure are further realized to investigate the gas permeability change of fractured sample. The correlation between gas permeability variation and fracture opening is analyzed.

## Highlights

- An original direct shear test is performed in order to investigate the creep deformation and permeability evolution of sound and fractured claystone.
- The creep strain rate is not significantly enhanced by the creation of fracture and it is mostly controlled by frictional sliding along fracture surface.
- The shear sliding leads to a normal opening of fracture leading to a significant increase of gas permeability.
- There is a clear correlation between gas permeability evolution and fracture opening and closure.

**Keywords** Gas permeability · Direct shear test · Creep · Confining pressure · claystone

## 1 Introduction

Underground geological repository is considered as a feasible solution for reversible disposal of radioactive waste. In a number of countries, clayey rocks are selected as a potential geological barrier. In the French project, a future

disposal site is envisaged in the Callovo-Oxfordian (COx) claystone in the East region of France. An underground research laboratory (URL) has been constructed to investigate thermo-hydromechanical responses of various storage components in real conditions. A synthesis on the feasibility evaluation of such a geological repository can be found in Andra (2005).

In this context, oxidation of metal components can produce hydrogen gas which can diffuse through engineered and geological barriers. An increase of gas pressure can induce claystone cracking. At the same time, excavation of galleries and boreholes can also generate damaged and fractured zones (EDZ) (Armand et al. 2014). The existence of EDZ can enhance diffusion of water and gas (de La Vaissiere et al. 2015). It is, therefore, an important topic to investigate

✉ J. F. Shao  
jian-fu.shao@polytech-lille.fr

<sup>1</sup> Key Laboratory of Ministry of Education for Geomechanics and Embankment Engineering, Hohai University, Nanjing 210098, China

<sup>2</sup> University of Lille, CNRS, Centrale Lille, UMR9013-LaMcube, 59000 Lille, France

<sup>3</sup> Andra, 92298 Chatenay Malabry, France

interactions between gas flow and claystone deformation, damage and cracking.

A number of previous studies have been devoted to gas flow in clay and clayey rocks. It is not our intention to deliver an exhaustive review and only some representative works in connection with the present one are mentioned. For instance, coupled effects of water content, dry density and confining pressure on gas permeability of a compacted bentonite-sand mixture, studied as engineered barrier, have been investigated in Liu et al. (2015a, b). Some studies have been devoted to the characterization of gas breakthrough pressure and its correlation with pore volume distribution (Song et al. 2016). Impacts of bentonite fraction, water content and dry density on the compaction and sealing properties of bentonite/claystone mixture have been recently studied in Zeng et al. (2021). Some authors have investigated wetting–drying cycle effects on the COx claystone permeability and elastic modulus in Duan et al. (2021) and Zeng et al. (2021). More classically, variations of COx permeability during triaxial compression tests have been characterized in terms of induced volumetric strain or damage (Yang et al. 2010; Giot et al. 2018). Some authors have investigated gas and water permeability variations of macro-cracked COx claystone samples under hydrostatic compression (Davy et al. 2007). Effects of creep deformation on gas permeability of COx claystone have also been considered in Liu et al. (2016, 2018). Some authors have investigated permeability characteristics of mudstone cap rock and inter-layers in bedded salt formations (Liu et al. 2015c).

However, in most previous studies, simple and conventional mechanical loading paths have been considered, mainly including hydrostatic and triaxial compression. In the case of fractured samples, artificial fractures were usually generated by indirect tension loading or simply by putting two semi-pieces together to form an interface. In real situations, rock layers are subjected to more complex loading paths. In the context of underground cavities, compressive stresses are dominating. Rock cracking and fracturing are generally created by the maximum shear stress exceeding the critical shear strength. Furthermore, the created fractures are subjected to frictional sliding under given normal effective stress. It is, therefore, important to investigate permeability evolution of rock subjected to compressive shearing before, during and after fracturing. This is the main objective of the present study. Some experimental methods have been proposed to measure the permeability of clayey soils in a direct shear device, for instance (Terzaghi et al. 1996). However, there are significant differences between those previous studies and the present one. In soils, it is relatively easy to create a fracture and to perform shear test with the help of classical shear box. For hard claystone, it is difficult to create natural fracture under direct shear loading. Furthermore, as the permeability of claystone is much lower than that of clayey soils, the measurement of permeability requires

a high injection pressure and then a good lateral sealing of sample. In the present study, we shall develop an original experimental method allowing the creation and shearing of fracture in a cylindrical sample under a given confining stress. This method is applied to investigate deformation, fracturing and gas permeability evolution of the COx claystone during a direct shear test. The tested sample is first subjected to a hydrostatic stress. A shear stress is then applied to the sample with measurement of shear strain, permeability before and after the creation of fracture. Several shear creep steps are also conducted to investigate the impact of time-dependent deformation of gas permeability. Impacts of confining pressure unloading–reloading on gas permeability variations are also investigated.

## 2 Material and Experimental Method

### 2.1 Material and Sample Preparation

The tested material is the Callovo-Oxfordian (COx) claystone cored from the main level of the Underground Research Laboratory (URL) at Bure in France operated by the French national agency for radioactive waste management (Andra). This clayey rock is mainly constituted of clay minerals, carbonate, quartz and some minor components (Robinet et al. 2012). The average clay fraction is about 40–45%, carbonate (mostly calcite) about 25–35% and quartz about 30%. The minor minerals include pyrite and siderite. The porosity is in the range of 14–20%. The natural water content of drilled cores ranges between 5 and 8%. In spite of its relatively high porosity, the average field permeability of the COx claystone is very low and ranges from  $5 \times 10^{-20}$  to  $5 \times 10^{-21}$  m<sup>2</sup>, due to the small mean pore diameter which is about 20 nm (Armand et al. 2017).

Cylindrical samples tested in this study are cored from big cores of 300 mm in length and 78.5 mm in diameter with the reference EST58123. It is known that the COx claystone exhibits a structural anisotropy (Armand et al. 2017). Its thermal, hydraulic and mechanical properties are dependent on loading orientation with respect to bedding planes. A number of previous studies have been devoted to that topic (Zhang et al. 2012; Liu et al. 2015e; Zhang et al. 2019). In this study, the emphasis is put on the creep deformation and gas permeability evolution under shear loading. The effect of anisotropy is not taken into account. Therefore, all cylindrical samples are cored in the perpendicular direction to the bedding planes. The average size of samples is 40 mm in length and 37.5 mm in diameter. According to previous results of microscopic analysis (Robinet 2008), the average size of mineral grains (mainly calcite and quartz) is smaller than 100 μm and the mean pore diameter is about 20 nm. Therefore, the size of samples seems to be large enough

to represent a representative volume element of the COx claystone. Two sample ends are polished and rectified to be parallel each to other. The sample preparation is completed with caution to minimize the alteration of water content of cores. Sample lateral surface is protected and exposure time to atmosphere is minimized. All samples are sealed in plastic bags and stored in a tank filled with nitrogen at a pressure of 2 bars and under a room temperature of about 23 °C.

In the present study, only gas permeability is investigated on partially saturated samples. All tested samples are not resaturated or desaturated. We use a sample preparation procedure to avoid as much as possible the modification of initial water content of drilled cores. More precisely, for each prepared sample, two or three small cut pieces are collected and used for the measurement of water content. For this purpose, the mass of each piece is weighed on a balance with a precision of 0.001 g. It is then placed inside an oven for being dried at 105 °C. When the mass variation between two successive measurements in a 24 h interval is less than 0.1%, it is assumed that the piece is fully dried. The corresponding initial water content of sample  $w_{\text{initial}-20^{\circ}\text{C}}$  is calculated by the following relation:

$$w_{\text{initial}-20^{\circ}\text{C}} = \frac{m_{\text{initial}-20^{\circ}\text{C}} - m_{\text{dried}-105^{\circ}\text{C}}}{m_{\text{dried}-105^{\circ}\text{C}}} \times 100\%, \quad (1)$$

where  $m_{\text{initial}-20^{\circ}\text{C}}$  is the initial sample mass at room temperature and  $m_{\text{dried}-105^{\circ}\text{C}}$  is the dried one at 105 °C. For the samples tested in this study, the average initial water content is about  $7.1 \pm 0.5\%$ . This value is very close to the natural water content of big cores as mentioned above.

## 2.2 Experimental Device and Procedure

In this study, a home-designed autonomous and auto-compensated triaxial testing system is used (Liu et al. 2015d). This one is composed of a conventional triaxial cell to apply confining pressure, an upper pressure chamber to generate axial force on the piston, and a flow circuit of interstitial fluid. This system is also equipped with an auto-compensation chamber inside the upper part of the cell, which is connected to confining fluid filling the main chamber. Therefore, the application of confining pressure does not generate any additional force on the piston. The axial force applied on the piston generates a pure deviatoric stress which is equal to the difference between axial and radial stresses. The axial force and confining pressure are both controlled by two independent pressure generators.

Moreover, to conduct direct shear test on a cylindrical sample, an original experimental device was designed and used in this study. The objective is first to create a planar fracture along the height of a cylindrical sample and then to apply shear stress along the created fracture surface. A

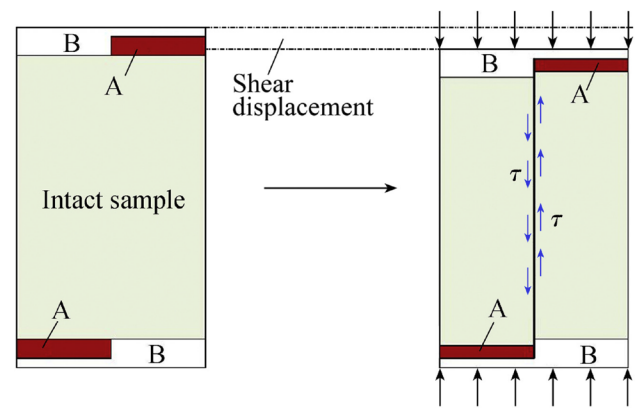


Fig. 1 Illustration of principal ideas for planar fracture creation and direct shear test (Yang et al. 2017; Liu et al. 2021)



Fig. 2 Picture of a COx sample fractured using the direct shear device

detailed description of the device can be found in Yang et al. (2017) and Liu et al. (2021). The principal ideas of fracture creation and shear test is illustrated in Fig. 1. Two especial cylindrical discs with the same diameter as the sample are fabricated. Each one is composed of two semi-discs made of different materials, a soft one (A) and a stiff one (B). The two semi-discs are placed in opposite positions at the top and bottom surfaces of the sample. Due to a large stiffness difference between the two semi-discs, an axial displacement generated by the cell piston creates a shear stress along the central plane of the sample, allowing the creation of a planar fracture and subsequently, the application of a shear stress

along the fracture. The axial relative displacement between two half cylinders of the sample, measured by two LVDTs, can be converted to the shear strain of fracture. At the same time, the relative variation of sample diameter ( $\Delta D/D$ ) is measured by a self-designed circumferential strain ring, and it can be used to evaluate the normal opening of the fracture. In Fig. 2, one shows the picture of a COx claystone sample containing a planar fracture created by using this specific direct shear device. Furthermore, under both hydrostatic and deviatoric stresses, it is possible to inject gas or water through the interstitial fluid circuit to determine permeability of sound or fractured sample. The whole set of system can be placed inside a thermally controlled chamber in order to regularize temperature throughout test. All monitoring and measuring data are collected in an acquisition computer.

### 2.3 Experimental Procedure

To meet the multiple objectives of the present study, a specific experimental procedure is designed. The whole test is composed of the following three main phases:

- Phase 1: gas breakthrough pressure of sound sample;
- Phase 2: gas permeability evolution during shear creep test of sound sample;

- Phase 3: gas permeability evolution of fractured sample under direct shear and confining pressure

The main test steps are summarized in Fig. 3. More detailed descriptions of each phase are presented below.

In the phase 1, the confining pressure is first increased to a desired value, for instance 12 MPa. Nitrogen gas is then injected into the sample. The inlet pressure is step-by-step raised until the gas flow is detected by a gas meter and the gas bubbles are observed at the outlet side which is in contact with the atmospheric pressure. The corresponding injection gas pressure is considered as the breakthrough pressure of the intact sample.

In the phase 2, a direct shear creep test is performed with gas permeability measurement. More precisely, the confining stress is kept to a constant value and the gas injection pressure is maintained at the breakthrough one. With the help of specific device presented above, shear stress is increased to about 50% of the estimated shear strength using a constant axial strain rate of  $10^{-6}$ /s. By keeping the shear stress at this level, a shearing creep step is realized until the stabilization of axial or shear strain. Then, the shear stress is increased to about 90% of the estimated shear strength with the same strain rate. A second shearing creep step is conducted at this shear stress level. During each shearing creep step, gas permeability is measured. Furthermore, under the

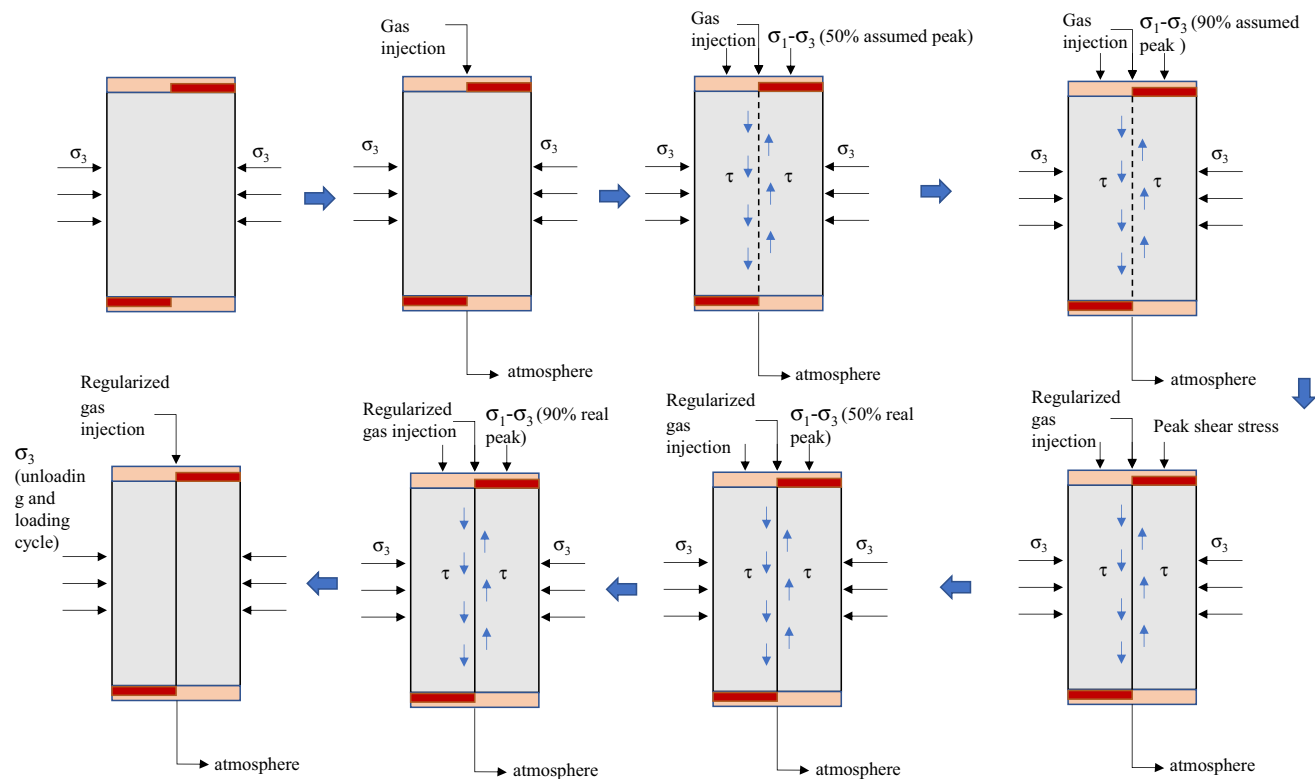


**Fig. 3** Schematic illustration of different loading steps of a complete direct shear test with gas permeability measurement

constant confining stress and injection gas pressure, the shear stress is increased by controlling the axial strain rate until the creation of a planar fracture in the sample. After that, the shear stress is decreased to about 45% of the actual shear strength obtained while the confining stress and injection gas pressure are kept unchanged. A post-peak shearing creep step is realized with gas permeability measurement at this shear stress level. After then, the shear stress is again raised to 80% of the actual peak value to perform a second creep step of the fractured sample always with gas permeability measurement.

The phase 3 is mainly devoted to investigate the effect of confining stress on the gas permeability evolution of fractured sample. To this end, the shear stress is first completely unloaded. The confining pressure is step-by-step decreased to a low value, for instance 2 MPa, and the gas permeability is measured at each unloading step. During these steps, the gas injection pressure is continuously adjusted. If this one becomes higher than the confining pressure, it is then decreased accordingly. Finally, the confining stress is step-by-step increased to its initial value and the gas permeability is measured at each reloading step. Again, the gas injection pressure is adjusted with respect to that of confining stress and breakthrough pressure.

## 2.4 Gas Permeability Measurement

We know that gas permeability is affected by the saturation degree of tested claystone, which can be calculated on basis of water content, porosity and specific gravity. For simplicity, in this study, the water content is used to evaluate the saturation of sample. In this study, the steady-state flow method is adopted for gas permeability measurement. The gas pressure is measured by a high precision gas pressure sensor installed at the inlet, while the injected gas volume is measure by a high precision gas flow meter of Bronkhorst. And the outlet remains atmospheric pressure. The steady-state flow method is adopted. According to Darcy's law, the following relation is used to calculate the gas permeability:

$$k = \frac{Q}{A} \frac{2\mu L P_{\text{out}}}{(P_{\text{in}}^2 - P_{\text{out}}^2)}, \quad (2)$$

where  $k$  ( $\text{m}^2$ ) is the gas permeability,  $L$  (m) the length of sample,  $A$  ( $\text{m}^2$ ) the cross-sectional area,  $Q$  ( $\text{m}^3/\text{s}$ ) the gas flow volumetric rate,  $\mu$  the viscosity coefficient for nitrogen ( $\mu = 1.76 \times 10^{-5} \text{Pa} \cdot \text{s}$  at  $20^\circ\text{C}$ ),  $P_{\text{in}}$  (Pa) the inlet pressure, and  $P_{\text{out}}$  (Pa) the outlet pressure taken as the atmospheric one in this study.

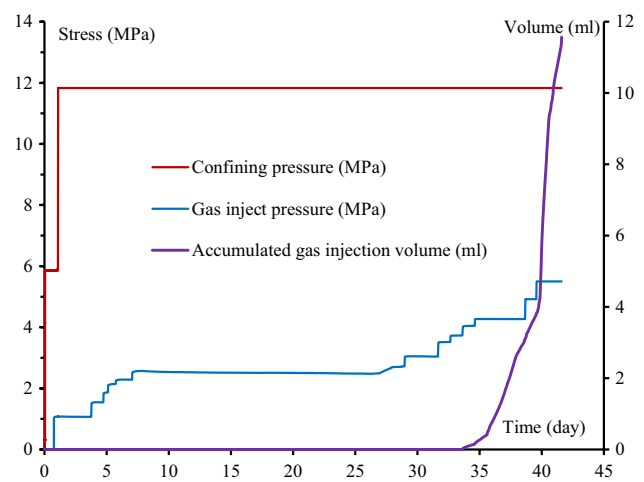
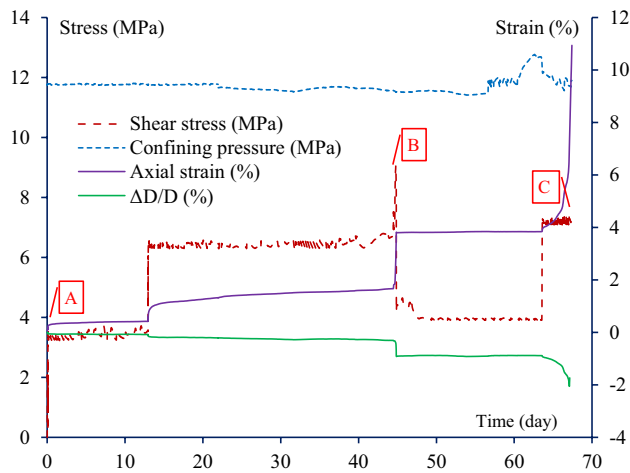


Fig. 4 Loading path of confining stress, variations of gas injection pressure and accumulated flow volume with time

## 3 Experimental Results and Discussion

### 3.1 Gas Breakthrough Pressure Under Hydrostatic Pressure

In this study, we have selected a representative test performed under a confining stress of 12 MPa. As mentioned above, the gas breakthrough pressure under hydrostatic stress is determined in the phase 1 of test. In Fig. 4, one shows the loading path of confining stress and the variations of gas injection pressure and flow volume with time. It is found that when the injection pressure is smaller than 3.7 MPa, there is almost no gas flow through the sample, and the accumulated gas injection volume remains negligible. As the inlet gas pressure becomes higher than 3.7 MPa, the flow meter detects a small value of gas flow. However, no bubble overflow at the outlet end is observed with the observation water cup. Then, the injection gas pressure continues to increase and the gas flow rate shows an upward trend. When the injection pressure is close to 5.5 MPa, the gas flow rate rapidly increases and an obvious gas flow is detected at the outlet end of sample. Therefore, for this test, the breakthrough pressure is about 5.5 MPa. However, it is important to point out that despite all the caution taken, the tested sample is still partially desaturated and disturbed during drilling and preparation steps. In general, it is easier for gas to flow through the sample than the in-situ saturated  $\text{CO}_2$  layer. Therefore, the gas breakthrough pressure obtained in the present test is probably lower than that in the real in situ conditions.



**Fig. 5** Variations of shear stress, axial and radial strains with time during different loading steps under a confining pressure of 12 MPa

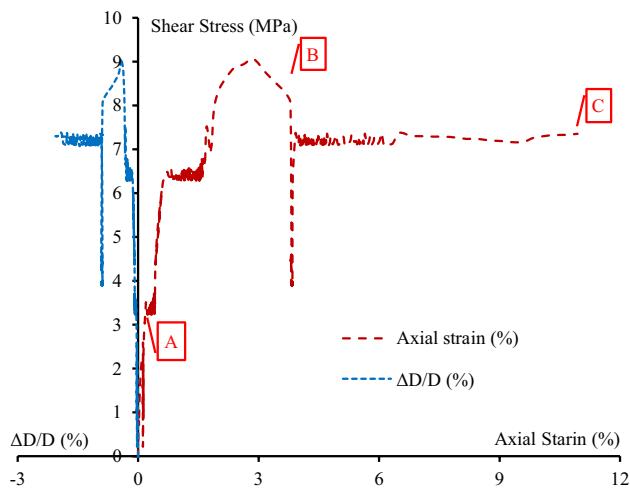


**Fig. 6** Shear stress versus accumulated axial and radial strains in a direct shear creep test under a confining pressure of 12 MPa

### 3.2 Shear Creep Deformation and Fracture

In the phase 2, the shear stress is step-by-step applied between two half parts of the sample, respectively, located under the hard and soft semi-disc. Time-dependent strains and gas permeability are measured at different loading steps and during creep time.

The variations of shear stress and strains with time are presented in Fig. 5, while the accumulated strains versus shear stress are given in Fig. 6. At the first step, the confining stress and gas pressure are kept constant, respectively, at 12 MPa and 5.5 MPa. The shear stress is successively raised to 50% and 90% of the estimated peak value based on a preliminary test. Both axial and radial strains are continuously measured. Due to the specific testing device

presented above, the axial strain is mainly induced by the relative displacement of the half-part of sample under the stiff semi-disc with respect to the other part under the soft semi-disc. Therefore, the axial strain can also be interpreted as the shear strain induced by the shear stress. At the same time, the radial strain is measured in terms of the relative variation of sample diameter  $\Delta D/D$  (positive value for contraction and negative value for dilation). It is found that the axial strain is significantly larger than the lateral one. The later remains negative during the whole duration of test. This indicates that the applied shear stress induces a continuous radial dilation of sample. Moreover, at each level of shear stress, creep strains are also measured. It is observed that at 50% of the estimated peak strength, the axial and lateral creep strains of intact claystone sample remain very small and quickly reach stationary values. The creep strains become clearly higher when the shear stress reaches 90%. Therefore, the creep deformation of the intact claystone sample is obviously enhanced by the shear stress level.

At the end of second creep step, the shear stress is increased to its peak value and a planar fracture passing through the sample is created. This operation is realized by controlling the axial displacement to avoid the brittle failure of sample. During this step, one observes a sudden rise of the axial strain due to the relative sliding along the created fracture surface. At the same time, the shear sliding also induces a rapid increase of radial dilation strain, or equivalently normal opening of fracture. This indicates that the fracture surface is not smooth but rough due to the existence of asperities. The shear sliding-induced normal opening is controlled by the fracture surface roughness.

Once the planar fracture is created, the shear stress is decreased to 45% of its actual peak value for performing the first creep step of fractured sample. It is interesting to notice that nearly no variation of axial and radial strains is measured during the unloading of shear stress, indicating that the fracture is locked by the confining stress and surface friction. During the creep period of fractured sample, compared with that of the intact one at a similar relative shear stress level (50%), no clear differences between two states are observed. It seems that the presence of planar fracture does not obviously enhance the shear creep deformation. This is mainly due to the relatively high confining stress (12 MPa) which induces a quite important frictional resistance to the shear creep sliding. The shear stress is finally increased to 80% of the actual shear strength to carry out the second creep step of fractured sample. Clearly, an accelerated creep deformation phase is obtained. The shear (axial) strain is rapidly multiplied by three times. At the same time, the radial dilatation strain is also accelerated.

For a quantitative analysis, the axial and radial creep strains rates are also calculated and presented in Fig. 7. In consistency with the accumulated creep strains given in

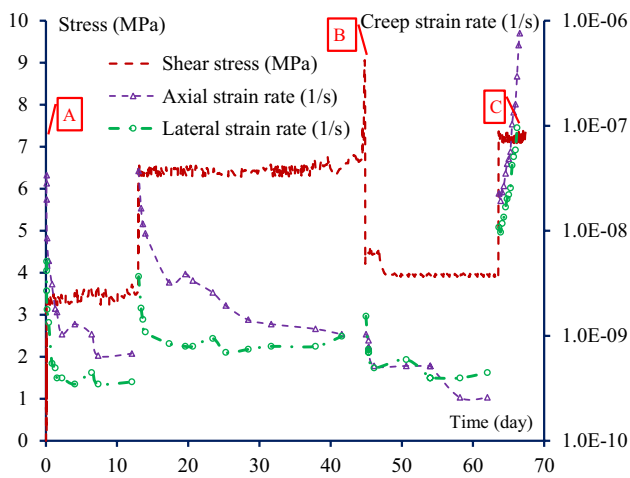


**Fig. 7** Variations of creep strain rates during different loading steps under a confining pressure of 12 MPa

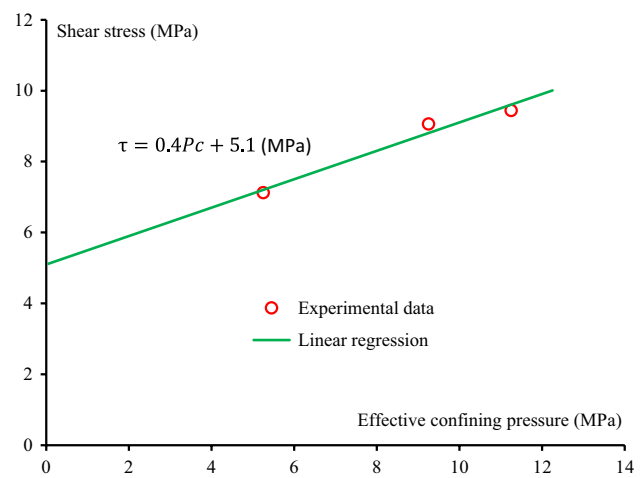


**Fig. 8** Shear strength approximation of COx claystone subjected to direct shear tests under different effective confining (normal) stresses

**Table 1** Values of peak shear strength of COx claystone in direct shear tests under different confining stresses

Samples number	Confining stress $P_c$ /MPa	Mean gas pressure $P_g$ /MPa	Effective confining stress $P_c^{eff}$ /MPa	Shear strength $\tau_{max}$ /MPa
C15	6.0	0.75	5.25	7.12
C16	12	0.75	11.25	9.44
C17	12	2.75	9.25	9.06

Fig. 5, before the creation of planar fracture, the axial and radial creep rates of the intact sample both increase with the applied shear stress. The initial axial creep strain rate is higher than that of the radial one. At the same time, the axial creep strain rate decreases more slowly with time than the radial one. After the creation of fracture (point B in the figure), at 45% of the actual peak shear strength, the creep strain rates are even slightly smaller than those of the intact sample obtained at 50% of the estimated shear strength. This confirms that under low shear stress and high confining pressure (12 MPa), the creep deformation is not obviously enhanced by the existence of fracture. However, when the shear stress is at 80% of the peak shear strength, the creep strain rates are amplified by several orders of magnitude, leading to a large accumulated axial strain together with an important radial dilation given in Figs. 5 and 6.

The shear fracture strength is also investigated. It is noticed that for the formulation of strength criteria of materials, stress invariants, such as mean stress, generalized deviatoric stress and Lode angle, are generally used. However, for the description of shear strength of fractures, interfaces and joints, it is physically preferable to adopt the normal and shear stresses defined in the local coordinates frame. Indeed,

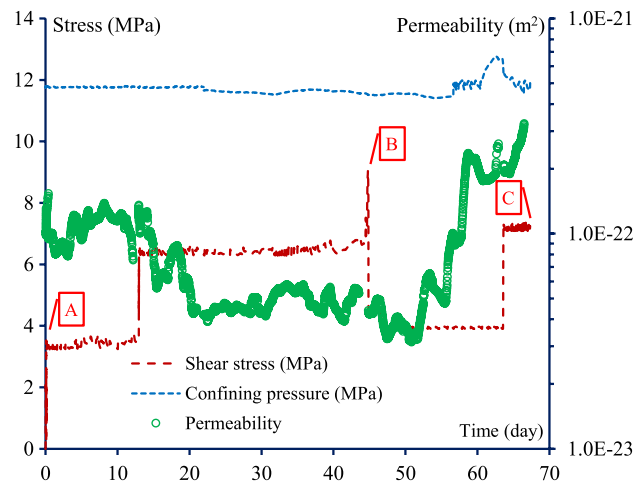


**Fig. 9** Variations of gas permeability with time during direct shear test under a confining pressure of 12 MPa

the shear strength of such discontinuous surfaces is usually expressed as a function of the normal stress. In case of saturated fracture, an effective normal stress is defined. In the present study, the following method is adopted. Three direct shear tests are performed of COx claystone samples: the first one with a confining stress of 6 MPa and a gas injection pressure of 1.5 MPa, the second one with a confining stress of 12 MPa and a gas injection pressure of 1.5 MPa, and the third one is that presented above with a confining pressure of 12 MPa and a gas injection pressure of 5.5 MPa. Furthermore, to define the shear strength of saturated fractures in the COx claystone, the widely used Terzaghi's concept is adopted to define the effective normal stress. However, as the gas pressure is not uniform along the sample height, a mean value is used to calculate the effective confining stress. In

Table 1, the values of peak shear stress leading the creation of planar fracture are reported. With these values, in Fig. 8, the peak shear stress is plotted as a function of effective confining pressure which can be seen as the effective normal stress applied onto the fracture. It is found that as a first approximation, a linear failure criterion can be identified. The values of friction angle and cohesion can be estimated and one gets  $c = 5.1$  MPa and  $\phi = 24^\circ$ .

### 3.3 Gas Permeability Evolution Under Shearing

In Fig. 9, the evolution of gas permeability is presented. The initial value of permeability of the tested sample is about  $1.5 \times 10^{-22}$  m<sup>2</sup>. During the first creep step under 50% of the estimated peak shear strength, there is no significant variation of permeability despite a small dilation of radial strain shown in Fig. 5. When the shear stress is increased to 90% in the second creep step, there is even a slight decrease of gas permeability from  $1.5 \times 10^{-22}$  to  $4.3 \times 10^{-23}$  m<sup>2</sup>, followed by a relatively stationary period. At the same time, the radial strain dilation continues to slowly increase (see Fig. 5). Such results indicate that no localized pathways are created to enhance gas flow through the sample. The small decrease of permeability can be due to the overall volumetric compaction of sample due to high confining pressure. At the end of the second creep step, the shear stress is increased to its peak strength and a longitudinal planar fracture is created, inducing a sudden increase of both axial and radial strains. After then, during the first creep step of the fractured sample at 45% of the actual shear strength, there is a rapid raise of gas permeability to reach a value of about  $2.5 \times 10^{-22}$  m<sup>2</sup>, in consistency with the continuous increase of radial strain dilation. During the second creep step of the fractured sample at 80% of the real peak shear strength, important fluctuations are observed around an average value of  $2.5 \times 10^{-22}$  m<sup>2</sup>. Despite a rapid radial dilation raise (see Fig. 5), no significant increase of permeability is observed, which only increases from  $1.9 \times 10^{-22}$  to  $3.2 \times 10^{-22}$  m<sup>2</sup>. This can probably be a consequence of the progressive self-sealing of fracture due to fine clay particles deposit during shearing process, causing an increase of tortuosity. As a partial conclusion, it seems that the gas permeability variation is dominantly controlled by the creation of localized fracture which represents a privileged pathway for gas flow. The role of fracture in enhancing gas permeability is influenced by its tortuosity. However, compared with a typical over-consolidated clay which is known to dilate during shearing, leading an increase of permeability, the deformation mechanism and permeability evolution of hard claystone during shearing under high confining stress seem to be more complex. Indeed, the micro-structure and fracture surface morphology are quite different between over-consolidated clay and hard claystone. Under a high confining stress such as 12 MPa

used in this study, shearing does not systematically induce overall dilation. In a fractured sample, the relationship between normal dilation (or compaction) and shear strain also depends on fracture surface roughness. Moreover, the correlation between gas permeability and volumetric dilation is also more complex than for water permeability. In many cases, the gas permeability is enhanced by different types of privileged pathways such as thin cracks and interfaces. And this enhancement is not systematically related to overall dilation. Therefore, further investigations are still needed to quantify the gas permeability evolution with stress, strain and crack states.

### 3.4 Effect of Confining Stress Variation on Gas Permeability of Fractured Sample

In the phase 3, the emphasis is put on the permeability dependency of fractured sample on the variation of confining pressure. For this purpose, unloading–reloading cycles of confining and gas injection pressures are realized. As shown in Fig. 10, the confining pressure is decreased from 12 to 5.8 MPa, while the gas injection pressure is kept at 5.5 MPa. It is seen that the gas permeability remains quasi unchanged during the first period of unloading and then suddenly increases by almost three orders of magnitude, from  $2.5 \times 10^{-22}$  to  $3.5 \times 10^{-19}$  m<sup>2</sup>. This indicates that a privileged flow pathway is created due to the opening of fracture induced by the confining pressure decrease. After then, both the confining and gas injection pressures are decreased, respectively, to 2 MPa and 1.8 MPa. After a period of deformation stabilization, they are step-by-step reloaded, in an alternative manner, respectively to 12 MPa and 5.8 MPa, as shown in Fig. 11. In the first step, the confining pressure is raised while the gas injection pressure is kept constant, the

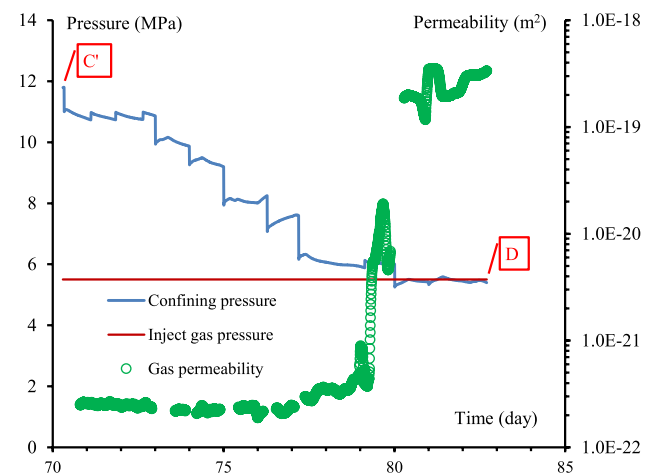
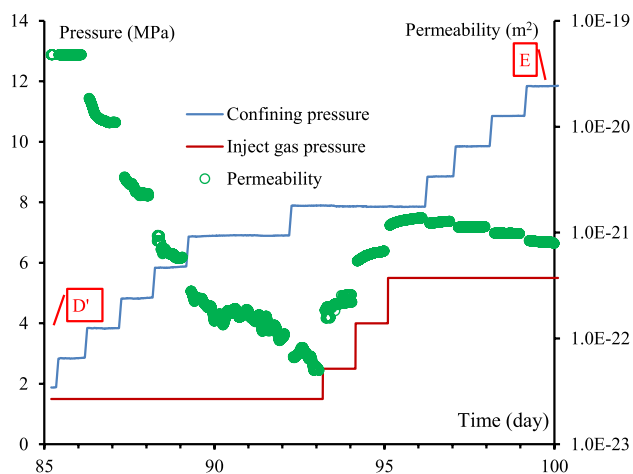
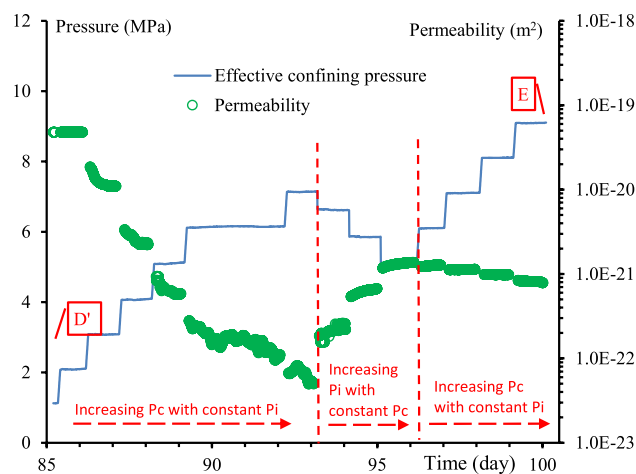


Fig. 10 Permeability evolution of fractured sample during unloading of confining pressure





**Fig. 11** Permeability evolution of fractured sample during reloading of confining pressure



**Fig. 13** Permeability evolution of fractured sample in terms of Terzaghi effective confining pressure reloading

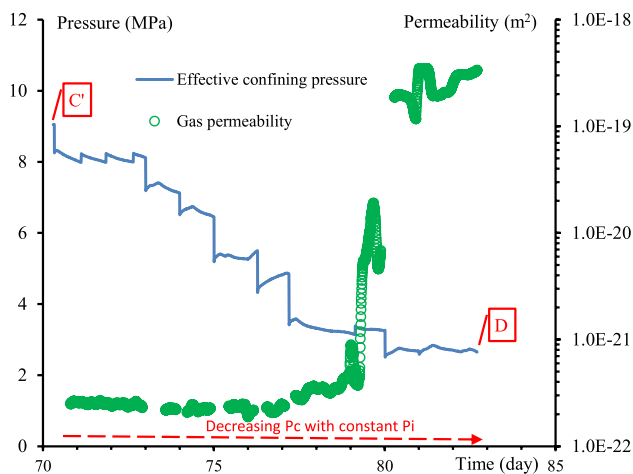


**Fig. 12** Permeability evolution of fractured sample in terms of Terzaghi effective confining pressure unloading

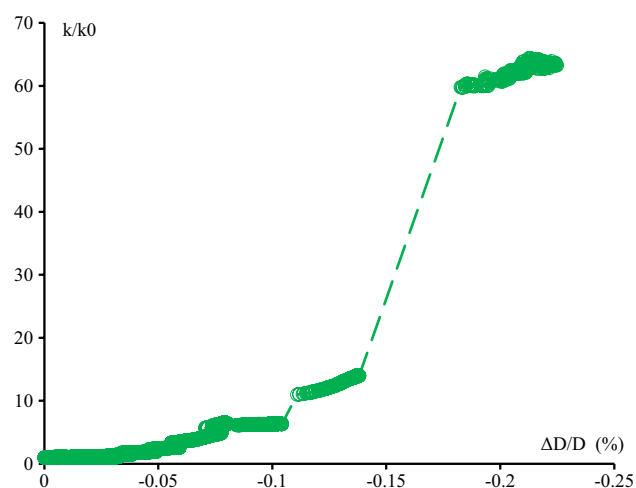


**Fig. 14** Relative permeability variation versus radial dilation of sample C16 during unloading of confining pressure with a gas injection pressure of 1.5 MPa

gas permeability continuously and significantly decreases by about three order of magnitude, from  $4.8 \times 10^{-20}$  to  $5.0 \times 10^{-23} \text{ m}^2$ . During the second step, the gas injection pressure is raised to 5.5 MPa by keeping the confining pressure unchanged, there is an obvious increase of permeability, from  $5.0 \times 10^{-23}$  to  $1.4 \times 10^{-21} \text{ m}^2$ . In the third step, the confining pressure is increased again by holding the gas injection pressure at 5.5 MPa. This leads to a decrease of permeability, from  $1.4 \times 10^{-21}$  to  $7.8 \times 10^{-22} \text{ m}^2$ . But compared with the first step, the amplitude of permeability decrease is much less important. This indicates that the gas flow paths are largely closed by the confining pressure reloading during the first step and not fully recovered in the second step by the gas pressure reloading.

It is worth noticing that the confining and gas injection pressures are alternatively changed in this phase. To investigate their combining effects on the permeability variation, In Figs. 12 and 13, we present the gas permeability variations in terms of Terzaghi effective confining pressure (difference between confining pressure and mean value of gas injection and outlet pressures). One can observe an obvious correlation between the permeability variation and effective confining stress change. The decrease (or increase) of effective confining pressure leads to the increase (or decrease) of the gas permeability of fractured claystone sample.

These results presented above suggest that the gas permeability variation is not an reversible process during the unloading–reloading phases of Terzaghi effective confining

stress. This phenomenon can be related to several factors. The mechanical behavior of fractured sample under compression is not fully elastic and plastic deformation is produced during loading–unloading cycles. Creep strains continuously evolve between the unloading and reloading periods. This inelastic behavior should be taken into account in future study when developing theoretical models for the description of deformation and permeability variation.

Unfortunately, due to some technical troubles, the radial dilation strain was not measured during the phase 3. It is then not possible to provide a quantitative analysis on the relationship between the gas permeability variation and fracture dilation. However, to remediate this lack, in Fig. 14, the relationship between the permeability change and radial dilation during the unloading of confining pressure are presented for the sample C16 used in the shear test with the gas injection pressure of 1.5 MPa (see Table 1). Three variation stages of gas permeability can be observed. This one increases slowly with the radial dilation during the first stage. This is probably due to the fact that the privileged flow paths are not fully created. There is a rapid increase of permeability in the second stage due to the significant opening of fracture. In the third stage, the permeability continues to increase but with a much smaller rate than that of the first stage. It is not easy to give a definite explanation of this phenomenon. One may invoke a possible modification of fracture surface tortuosity due to the formation of clay particles. It is worth noticing that in the present study, the permeability variation is interpreted only in terms of deformation and stress state during shearing process. Other important phenomena can significantly affect the permeability (gas and water) evolution, in particular fracture healing due to dissolution, precipitation and other processes. These issues should be investigated in future studies.

## 4 Concluding Remarks

In this study, the creep deformation and permeability evolution have been investigated on sound and fractured states of the COx claystone subjected to direct shear loading. The main outcomes are summarized below.

The shear strength of COx claystone is influenced by effective confining pressure. As a first approximation, a linear shear strength criterion can be identified for the stress range considered in this study. Under a confining pressure of 12 MPa, the gas breakthrough pressure of the tested sample is about 5.5 MPa. This value should be smaller than that in the real in situ conditions due to the disturbances induced during core drilling and sample preparation.

The creep strain rate of the sound state (before creation of fracture) is generally quite small, say less than  $1 \times 10^{-9}$  /s. After the creation of planar fracture, the creep strain rate

remain small if the applied shear stress is low with respect to the peak shear strength, for instance 45%. The creep strain rate is amplified by several orders of magnitude when the shear stress is close to 80% of the peak shear strength. The deformation of fractured sample is mostly controlled by frictional sliding along fracture surface. The elastic shear strain is negligible. The plastic and viscoplastic shear sliding leads to an normal opening of fracture.

The initial value of gas permeability of tested sample is about  $1.5 \times 10^{-22}$  m<sup>2</sup>. The variation of gas permeability of the sound state during direct shearing is very small. The creation of planar fracture plays the key role in the evolution of gas permeability of fractured state. This one can be amplified by ten times during the creep steps of fractured sample. Furthermore, the gas permeability is strongly influenced by the effective confining pressure which is equivalent to the effective normal stress applied onto the fracture. The gas permeability increases when the effective confining pressure decreases and inversely. But the variation of gas permeability during unloading–reloading cycles of effective confining pressure is not entirely reversible. The permeability increase during unloading is more important than that during reloading. There is a clear correlation between the gas permeability change and normal opening of fracture which constitutes a privileged gas flow path. However, the gas permeability is also significantly affected by the roughness and tortuosity of fracture surface.

As perspectives, additional tests should be useful to confirm the main conclusion obtained in this study. Further investigations including microscopic analysis of shear fracture surface are necessary to identify effects of roughness, tortuosity and clay fines on gas permeability variation. To account for real disposal conditions, thermal effects on deformation, fracture and permeability variation of COx claystone under direct shear condition should also be taken into account. The fracture healing is also an important issue to be investigated.

**Acknowledgements** This work was jointly supported by the French National Agency for Radioactive Waste Management (Andra) to LaM-cube, and by the Chinese Scholarship Council to X. Chen. All these supports are gratefully acknowledged.

## References

- Andra (2005) Dossier 2005: synthesis—evaluation of the feasibility of a geological repository in an argillaceous formation, Meuse/Haute-Marne site
- Armand G, Leveau F, Nussbaum C, deLaVaissiere R, Noiret A, Jaeggi D, Landrein P, Righini C (2014) Geometry and properties of the excavation induced fractures at the Meuse-Haute-Marne url drifts. *Rock Mech Rock Eng* 47:21–41
- Armand G, Conil N, Talandier J, Seyedi DM (2017) Fundamental aspects of the hydromechanical behaviour of Callovo-Oxfordian

- claystone: from experimental studies to model calibration and validation. *Comput Geotech* 85:277–286
- Davy CA, Skoczylas F, Barnichon JD, Lebon P (2007) Permeability of macro-cracked argillite under confinement: gas and water testing. *Phys Chem Earth Parts A/B/C* 32:667–680
- de La Vaissiere R, Armand G, Talandier J (2015) Gas and water flow in an excavation-induced fracture network around an underground drift: a case study for a radioactive waste repository in clay rock. *J Hydrol* 521:141–156
- Duan ZB, Skoczylas F, Wang CR, Talandier J (2021) Hydric cycle impacts on cox argillite permeability and young's modulus. *Rock Mech Rock Eng* 54:1129–1147
- Giot R, Auvray C, Conil N, deLaVaissiere R (2018) Multi-stage water permeability measurements on claystone by steady and transient flow methods. *Eng Geol* 247:27–37
- Liu JF, Skoczylas F, Talandier J (2015a) Gas permeability of a compacted bentonite-sand mixture: coupled effects of water content, dry density, and confining pressure. *Can Geotech J* 52:1159–1167
- Liu JF, Song Y, Skoczylas F, Liu J (2015b) Gas migration through water-saturated bentonite-sand mixtures, cox argillite, and their interfaces. *Can Geotech J* 53:60–71
- Liu W, Li YP, Yang CH, Daemen JJK, Yang Y, Zhang GM (2015c) Permeability characteristics of mudstone cap rock and interlayers in bedded salt formations and tightness assessment for underground gas storage caverns. *Eng Geol* 193:212–223
- Liu ZB, Shao JF, Xie SY, Secq J (2015d) Gas permeability evolution of clayey rocks in process of compressive creep test. *Mater Lett* 139:422–425
- Liu ZB, Xie SY, Shao JF, Conil N (2015e) Effects of deviatoric stress and structural anisotropy on compressive creep behavior of a clayey rock. *Appl Clay Sci* 114:491–496
- Liu ZB, Shao JF, Liu TG, Xie SY, Conil N (2016) Gas permeability evolution mechanism during creep of a low permeable claystone. *Appl Clay Sci* 129:47–53
- Liu ZB, Xie SY, Shao JF, Conil N (2018) Multi-step triaxial compressive creep behaviour and induced gas permeability change of clay-rich rock. *Geotechnique* 68:281–289
- Liu ZB, Shao JF, Zha WH, Xie SY, Bourbon X, Camps G (2021) Shear strength of interface between high-performance concrete and claystone in the context of a French radioactive waste repository project. *Geotechnique* 71:534–547
- Robinet J (2008) *Minéralogie, porosité et diffusion dans l'argilite du callovo-oxfordien de bure (meuse/haute-marne, france) de l'échelle centimétrique à micrométrique*. Ph.D. thesis, PhD thesis, Université de Poitiers, 2008 (Cited on page iii, 3, 4, 5, 153)
- Robinet JC, Sardini P, Coelho D, Parneix JC, Pret D, Sammartino S, Boller E, Altmann S (2012) Effects of mineral distribution at mesoscopic scale on solute diffusion in a clay-rich rock: example of the Callovo-Oxfordian mudstone (Bure, France). *Water Resour Res* 48:W05554
- Song Y, Davy CA, Troade D (2016) Gas breakthrough pressure (GBP) through claystones: correlation with FIB/SEM imaging of the pore volume. *Oil Gas Sci Technol* 71:51–77
- Terzaghi K, Peck RB, Mesri G (1996) *Soil mechanics in engineering practice*. Wiley, New York
- Yang DS, Billiotte J, Su K (2010) Characterization of the hydromechanical behavior of argillaceous rocks with effective gas permeability under deviatoric stress. *Eng Geol* 114:116–122
- Yang H, Xie SY, Secq J, Shao JF (2017) Experimental study and modeling of hydromechanical behavior of concrete fracture. *Water Sci Eng* 10:97–106
- Zeng ZX, Cui YJ, Talandier J (2021) Compaction and sealing properties of bentonite/claystone mixture: impacts of bentonite fraction, water content and dry density. *Eng Geol* 287:106122
- Zhang CL, Armand G, Conil N, Laurich B (2019) Investigation on anisotropy of mechanical properties of Callovo-Oxfordian claystone. *Eng Geol* 251:128–145
- Zhang F, Xie S, Hu D, Shao J-F, Gatmiri B (2012) Effect of water content and structural anisotropy on mechanical property of claystone. *Appl Clay Sci* 69:79–86

**Publisher's Note** Springer Nature remains neutral with regard to jurisdictional claims in published maps and institutional affiliations.